

Spatial effect on the external radiative recombination in thin-film near-field radiative energy converters

Dudong Feng, Shannon K. Yee, and Zhuomin M. Zhang*

George W. Woodruff School of Mechanical Engineering,
Georgia Institute of Technology, Atlanta, GA 30332, USA

*Corresponding Author: zhuomin.zhang@me.gatech.edu

ABSTRACT:

Following the trend of miniaturization, thin-film radiative energy converters are preferred as high-performance technologies for energy conversion and harvesting. Accurate modeling of the external radiative recombination is crucial to predict the performance of a thin-film near-field radiative energy converters. In this work, we demonstrate that the total external radiative recombination coefficient calculated by fluctuational electrodynamics apparently diverges from that by van Roosbroeck-Shockley when the cell thickness is less than 10 μm . A 400 nm InAs cell is configured with different geometric structures to illustrate the spatial effect on the external radiative recombination. The spatial profile of the local external radiative recombination coefficient can be significantly modified due to photon recycling in the far field and photon tunneling in the near field. In addition, the local external radiative recombination coefficient reduces as the local doping level approaches that of a degenerate semiconductor. Intrinsic internal quantum efficiency (IIQE) is newly defined to distinguish the thermal radiation and nonthermal radiation quantitatively. The ideal IIQE assumption leads to an overprediction of the maximum power density and maximum efficiency of a near-field thin-film thermoradiative cell for more than 10% compared to the result by using a real IIQE.

KEYWORDS: *spatial effect; local external radiative recombination coefficient; intrinsic internal quantum efficiency; thermal and nonthermal radiation; fluctuational electrodynamics; external luminescence*

I. INTRODUCTION

Due to the growing concerns of climate change and environment pollutions, conventional energy generation and conversion technologies are urgently required to be replaced by clean energy innovation. With the advantages of compact size and solid-state operation, radiative energy converters are considered as promising technologies to harvest waste heat and replace conventional heat pumps [1]. By tuning the photon chemical potential and the working temperatures, radiative energy converters can realize energy conversion between thermal radiation and electrical energy. There are four kinds of radiative energy converters. Thermophotovoltaic (TPV) cells generate electrical current by absorbing thermal radiation from hot objects; while thermoradiative (TR) cells generate electrical current by emitting thermal radiation to cold objects. In a likely manner, electroluminescent refrigerators (ELR) can cool the objects by emitting more luminescence to the surroundings; while negative electroluminescent refrigerators (NELR) can cool the surroundings by suppressing the luminescence from the refrigerators [2,3]. The wide application scenarios of radiative energy converters appeal to researchers to realize such devices and further improve their performance.

Near-field radiation can overcome the blackbody limit when the hot and cold objects are brought to subwavelength scale, where photons are allowed to tunnel across the vacuum gap through coupled evanescent waves from two surfaces. The enhancement of photon exchange by near-field radiation can potentially boost the performance of near-field radiative energy converters. Significant theoretical and experimental progress have been demonstrated in recent years [4-8]. Following the thin-film trend of optoelectronic device industries such as photovoltaic (PV) cells and light emitting diodes (LEDs), near-field radiative energy converters can also benefit from reducing the thickness of active materials in a cell or a refrigerator. Although the volumetric absorption or emission is proportional to the thickness of active materials, the nonradiative losses, such as Auger and Shockley-

Read-Hall (SRH) processes, are also reduced by thinning the active materials. Moreover, the near-field effect on the local absorption and emission due to surface electromagnetic resonance can only penetrate a small skin depth of the active materials [2,9]. By optimizing the thickness of a cell or a refrigerator, thin-film structures are usually preferred for near-field radiative energy converters [10,11].

Neglecting the nonradiative processes, the radiative recombination and photon absorption are the main optical processes in radiative energy converters. By applying the principle of detailed balance, radiative recombination of nonequilibrium semiconductor diodes can be depicted by van Roosbroeck-Shockley model [12,13]. Thereafter, Wurfel proposed a more precise expression, which is using a modified Bose-Einstein distribution derived from Fermi-Dirac distribution of free carriers in nonequilibrium semiconductor [14]. Trupke *et al.* summarized a general expression of external radiative recombination considering the multiple reflections from the front and back interfaces [15]. Although thin-film near-field radiative energy converters possess the same working mechanism as regular PV cells and LEDs, whether the conventional model can be applied required a rigorous investigation. DeSutter *et al.* investigated the external luminescence (external radiative recombination) and photon recycling in a near-field TPV cell using fluctuational electrodynamics (FE) [16]. However, the linkage between van Roosbroeck-Shockley model and FE is not explicitly discussed.

In this work, the external radiative recombination coefficient (ERRC) calculated by FE is compared with generalized van Roosbroeck-Shockley model to show the thin-film effect. The local ERRC represents the capability of generating or absorbing a photon at a given location. Geometric effect on the local ERRC is also studied for a thin-film radiative energy converter working at different configurations. The doping effect on the local ERRC due to Moss-Burstein shift is emphasized for

the radiative energy converters made of direct narrow bandgap semiconductors. Wurfel theoretically distinguished the thermal radiation and nonthermal radiation (radiative recombination) by introducing the photon chemical potential [14], and Karalis and Jonannopoulos quantitatively distinguish the thermal and nonthermal contributions of photon absorption and emission to the performance of a near-field TPV using temporal coupled-mode theory [17]. With the newly proposed concept of intrinsic internal quantum efficiency (IIQE), the spectral intensity of thermal radiation and non-thermal radiation for a near-field TR cell is calculated using FE as an example. The performances of the near-field TR cell using two models are compared to indicate the importance of considering all the effect on the radiative recombination, which is a significant contribution on the modeling of thin-film near-field radiative energy converters. For simplicity, the following investigations are mainly performed for TPVs and TRs. However, the results of these configurations can be extended to other radiative energy converters without doubt.

II. MODELING OF EXTERNAL RADIATION RECOMBINATION

Combining the fluctuation-dissipation theorem (FDT) with Maxwell's equations, FE establishes the relation between the strength of the random fluctuations of the charges and local equilibrium status at a point source. With the assistance of the dyadic Green's function, the electric and magnetic fields are given by [2,18]:

$$\mathbf{E}(\mathbf{r}, \omega) = i\omega\mu_0 \int_V \overline{\overline{\mathbf{G}}}^E(\mathbf{r}, \mathbf{r}', \omega) \mathbf{J}(\mathbf{r}', \omega) dV' \quad (1)$$

$$\mathbf{H}(\mathbf{r}, \omega) = \int_V \overline{\overline{\mathbf{G}}}^H(\mathbf{r}, \mathbf{r}', \omega) \mathbf{J}(\mathbf{r}', \omega) dV' \quad (2)$$

where $\overline{\mathbf{G}}^E(\mathbf{r}, \mathbf{r}', \omega)$ and $\overline{\mathbf{G}}^H(\mathbf{r}, \mathbf{r}', \omega)$ are the dyadic Green's function for electric and magnetic fields, respectively. $\mathbf{J}(\mathbf{r}', \omega)$ is the fluctuating current density representing the source of thermal radiation at location \mathbf{r}' with a given frequency ω .

Applying the Poynting theorem, the spectral thermal emission at a given z location is expressed as [2,18]:

$$q_\omega(z) = 2 \operatorname{Re} \left[\frac{i\omega^2}{\pi c^2} \int_V dV' \int_V dV'' \left(G_{xn}^E G_{ym}^{H*} - G_{yn}^E G_{xm}^{H*} \right) \langle J_m(\mathbf{r}', \omega) J_n(\mathbf{r}'', \omega) \rangle \right] \quad (3)$$

where c is the speed of light in vacuum. G_{xn}^E and G_{ym}^H are the tensor components of the electric and magnetic dyadic Green's function, respectively. m and n stand for the three orthogonal components ($m, n = x, y, z$). $J_n(\mathbf{r}', \omega)$ and $J_m(\mathbf{r}'', \omega)$ represent the fluctuating current at two different locations \mathbf{r}' and \mathbf{r}'' in the emitting medium. $\langle \rangle$ and $*$ denote the ensemble average and the complex conjugate operation.

If one can assign the equilibrium status (temperature and photon chemical potential etc.) and the contribution of the imaginary part of the permittivity to each excitation type (interband transition, phonon, and free carriers), the spatial correlation function of the fluctuating current is given by:

$$\langle J_m(\mathbf{r}', \omega) J_n^*(\mathbf{r}'', \omega') \rangle = \frac{\omega \epsilon_0 \delta_{mn} \delta(\mathbf{r}' - \mathbf{r}'') W_{J_m, J_n}}{\pi} \quad (4)$$

where ϵ_0 is the permittivity of vacuum. δ_{mn} is the Kronecher function based on the isotropic medium assumption and $\delta(\mathbf{r}' - \mathbf{r}'')$ is the Dirac delta function due to the locality of dielectric

function [18]. Assuming $\text{Im}(\varepsilon) = \text{Im}(\varepsilon_{ib}) + \text{Im}(\varepsilon_{nonrad})$, the product of imaginary part of dielectric function and modified Bose-Einstein term can be rewritten as [19]:

$$W_{J_m, J_n} = \text{Im}[\varepsilon_{ib}(\mathbf{r}'', \omega)] \Theta(\omega, T_{ib}, \mu) + \text{Im}[\varepsilon_{nonrad}(\mathbf{r}'', \omega)] \Psi(\omega, T_{nonrad}, 0) \quad (5)$$

where $\varepsilon_{ib}(\mathbf{r}'', \omega)$ and $\varepsilon_{nonrad}(\mathbf{r}'', \omega)$ are the contribution to the imaginary part of the dielectric function due to interband transition and nonradiative absorption (phonons and free carriers), respectively. T_{ib} and T_{nonrad} are the local equilibrium temperature of where the interband transition and nonradiative absorption happen, respectively.

The modified Bose-Einstein distribution is used to model the emitted spectral photons, which is given by:

$$\Psi(\omega, T, \mu) = \begin{cases} \left[\exp\left(\frac{\hbar\omega}{k_B T}\right) - 1 \right]^{-1}, & \omega < \omega_g \\ \left[\exp\left(\frac{\hbar\omega - \mu}{k_B T}\right) - 1 \right]^{-1}, & \omega \geq \omega_g \end{cases} \quad (6)$$

where k_B is the Boltzmann constant, \hbar is the reduced Planck constant. and $\omega_g = E_g/\hbar$ is the frequency that corresponds to the bandgap energy (E_g). T is the temperature in local equilibrium condition.

Plug Eq. (4) into Eq. (3) and extract the component due to interband transition. The external radiative recombination of a thin film to the air can be written as [20]:

$$N_\omega = \Psi(\omega, T, \mu) \Pi_{QE}(\omega, T) \int_0^{k_0} \frac{dk_{\parallel}}{2\pi^2} \sum_{\gamma=s,p} \left(1 - |R^\gamma|^2 - |T^\gamma|^2 \right) \quad (7)$$

where $\text{IIQE}(\omega, T) = \text{Im}[\epsilon_{ib}(\omega, T)] / \text{Im}[\epsilon(\omega, T)]$ is defined as the ratio of the number of photons emitted by interband transition to the number of total emitted photons. From the perspectives of absorption, the IIQE can also be understood as the ratio of the number of local generated electron and hole pairs due to interband transition to the number of total absorbed photon. R^γ and T^γ are the reflection and transmission coefficients of the thin film when light is incident from air. The superscript γ represents the polarization state of light (s or p). $k_0 = \omega/c$ is the vacuum wavevector. The parallel wavevector k_{\parallel} is defined as $k_{\parallel}^2 = k_x^2 + k_y^2$.

Similarly, the spectral heat flux of thermal emission and nonthermal emission (external luminescence) can be calculated as follows, respectively:

$$q_{\omega, \text{thermal}} = \hbar \omega N_{\omega} [1 - 1/\text{IIQE}(\omega, T)] \quad (8)$$

and

$$q_{\omega, \text{lum}} = \hbar \omega N_{\omega} \quad (9)$$

By applying Boltzmann approximation on the modified Bose-Einstein distribution in Eq. (7) and dividing Eq. (7) by the product of the local free carriers concentrations, the ERRC of a film can be written as:

$$B_{\text{FE}} = \int_{\omega_g}^{\infty} \frac{\text{IIQE}(\omega, T) \exp(-\hbar \omega / k_B T)}{n_i(T)^2 h} \int_0^{k_0} \frac{dk_{\parallel}}{2\pi^2} \sum_{\gamma=s,p} \left(1 - |R^\gamma|^2 - |T^\gamma|^2\right) d\omega \quad (10)$$

where n_i is the intrinsic carrier concentration of the semiconductor materials and h is the thickness of the cell. To be noted, the application condition of Boltzmann approximation depends on the

injected carrier density and doping level of the semiconductor materials. The error of Boltzmann approximation has been discussed in detail in Ref. [21].

To study the local ERRC, a multilayer fluctuational electrodynamics formalism is applied to a thin-film cell with a nonuniform mesh to calculate photon exchange between any semiconductor layer and external environment. Applying the similar method in Ref [22], the local ERRC is given by:

$$B(t) = \int_{\omega_g}^{\infty} B_{\omega}(t) d\omega = \int_{\omega_g}^{\infty} \frac{\text{IQE}(\omega, T_{\alpha}) \exp(-\hbar\omega/k_B T_{\alpha})}{n_i(T_{\alpha})^2 h_{\alpha}} \Upsilon_{\alpha}(\omega) d\omega \quad (11)$$

where t is the location of layer α in the cell. T_{α} and h_{α} are the temperature and thickness of layer α , respectively. Here, layer α is assumed at local equilibrium condition (temperature, dielectric function and photon chemical potential etc.). The function $\Upsilon_{\alpha}(\omega)$ is the fraction of photon at a given frequency from layer α to external environment, which can be calculated as follows [22].

$$\begin{aligned} \Upsilon_{\alpha}(\omega) = & \left(\frac{\omega}{c_0 \pi} \right)^2 \text{Re} \left\{ i \text{Im}(\epsilon_{\alpha}) \int_0^{\infty} k_{\parallel} dk_{\parallel} \right. \\ & \left. \times \int_{t-\Delta z_{\alpha}/2}^{t+\Delta z_{\alpha}/2} \left[F(\omega, k_{\parallel}, z, z_c^+) + F(\omega, k_{\parallel}, z, z_c^-) \right] dz \right\} \end{aligned} \quad (12)$$

where ϵ_{α} is the dielectric function of layer α . Δz_{α} is the thickness of layer α . z_c^+ and z_c^- are the front side and back side location of the cell. The detailed expression of the function F can be found in Ref. [16,22-24].

Based on the expression of external radiative recombination provided by Trupke *et al.*, a general expression of the ERRC can be derived by applying Boltzmann approximation on the generalized Planck equation [15]:

$$B_{\text{Trupke}} = \int_{\omega_g}^{\infty} \frac{\omega^2}{4\pi^2 c_0^2 n_i^2} A(\omega) \exp(-\hbar\omega/k_B T) d\omega \quad (13)$$

where $A(\omega)$ is the absorptance of the slab, which is derived based on geometric optics neglecting the directional emission of a thin film [15].

III. RESULTS AND DISCUSSION

While the method present above is general, an intrinsic InAs slab is chosen as the example to show the thin film effect on external radiative recombination coefficient. With a direct bandgap of 0.354 eV around room temperature, InAs is a perfect candidate material to transform energy between infrared radiative energy and electrical energy. The dielectric function of InAs is depicted by the summation of absorption due to interband transitions, lattice resonance (optical phonon), and free carrier absorption. Milovich *et al.* developed a comprehensive model to numerically calculate the dielectric function of InAs, which manifests a very good agreement with experimental data at different doping levels and temperatures [25]. Since the absorption edge of a narrow bandgap semiconductor can be affected under the heavily doped condition, the Moss-Burstein effect is also taken into consideration in this dielectric function model [25-27]. To be noted, the default temperature of InAs is set at 300 K for the discussion of the ERRCs.

A. Thin film effect on the external radiative recombination coefficient

Figure 1 exhibits the ERRC of a InAs slab standing in the air (shown in the subplot in Fig. 1), which is calculated by both FE and Trupke's method using Eq. (10) and Eq. (13), respectively. The ERRC of the InAs film calculated by FE captures the coherent feature when the film thickness is less than 10 μm ; while the result calculated by Trupke's method shows only a monotonical

decreasing as the film thickness increases because the geometric optics is used in this method, which neglects the phase information of the propagating electromagnetic waves in the medium [2]. The direction-dependent emission is approximated by normal emission. Clearly, the ERRC calculated by FE can align quite well with Trupke's method at a thick-film regime ($> 10 \mu\text{m}$) because the interference effect in the thin-film optics makes no difference for a thick medium and the emission intensity from the surface a thick medium is direction-independent. Therefore, Trupke's model works perfectly for conventional PV cells and LEDs but not for thin-film optoelectronic devices. Moreover, the near-field effect is completely neglected in Trupke's method. Nevertheless, the near-field effect is taken into account by FE, which should be used to model the external luminescence more accurately when the gap thicknesses of near-field radiative energy converters are reduced to the submicron scale.

B. Spatial effect on the local external radiative recombination coefficient

In the far-field regime, the net radiative heat flux from an object is the difference between the radiosity and irradiation. This irradiation is closely related with the surrounding configurations. Therefore, the net radiative heat flux of an object would be affected by its surroundings. Same conclusion can be applied to the external luminescence. Marti *et al.* have investigated the effect of different backside structures on the dark current of a solar cell, which is essentially the external radiative recombination if the charge transport loss and nonradiative processes are neglected [28]. Similar studies are also performed on the external luminescence and dark current of a near-field TPV cell in different configurations [16,21,29]. However, the spatial effect on the local ERRC has barely been investigated for thin-film radiative energy converters. In Fig. 2a, the spatial profile of the ERRC of a 400 nm intrinsic InAs cell is calculated for three different configurations, which are shown in the subplots. Compared to the cell configuration, the far-field TPV configuration has

an optimized plasmonic emitter made of 30 nm indium tin oxide (ITO) and a bulk tungsten [10], which is separated from the InAs cell with a 1 mm vacuum gap. In Fig. 2a, the spatial profile of the local ERRC shows a symmetric valley-shape for both cell and TPV configuration, which indicates there is potentially higher emission possibility of recombined photons at two ends of the cell rather than the middle of the cell. The spectral local ERRC of these two configurations are plotted in Fig. 2b and 2c. Most electron and hole pairs recombine and generate photons with energies from 0.354 eV to 0.45 eV due to the dominant contribution from interband transition in the dielectric functions. Owing to multiple reflections by the front and back interface in the cell configuration, these propagating photons formed a spatial coherent pattern of emission possibility from the cell. When the film thickness is at micro- or nanoscale, this spatial coherent pattern exists for not only local absorption but also local external radiative recombination, which can be explained by applying the local Kirchhoff's law to coherent absorption of a thin film [19,30]. Compared to the cell configuration, the generated propagating photons in the TPV configuration are more likely recycled by the cell due to the additional multiple reflection by the plasmonic emitter. Therefore, the two red spots in Fig. 2c are lower than those in Fig. 2b. In other words, the spatial profile of the local ERRC of the TPV configuration is reduced when compared to the cell configuration. Moreover, a TPV cell with a back gapped reflector (BGR) is also studied as an example because of its potentially better performance compared to the conventional TPV configurations in both far-and near-field regime [29,31,32]. This BGR structure is made of a 100 nm gold and a 10 nm vacuum gap between the gold film and the cell. To be noted, the dielectric functions of tungsten, ITO and gold can be found in Ref. [10] and [22]. By adding a BGR structure on the far-field TPV configuration, the spatial profile of the local ERRC is changed as shown in Fig. 2a. Figure 2d illustrates the dominant spectrum of generated photons is still close to the

bandgap of InAs. The emission possibility at the middle is higher than that at the front side of the cell in this TPV-BGR configuration. The rise of the spatial profile of the ERRC at the back of the cell is due to the photon tunneling effect between the gold film and the cell, which will be discussed in the next paragraph.

Strong near-field effect can affect the spatial profile of the ERRC of the TPV-BGR configuration. As shown in Fig. 3, the ERRC increases as the separation distance between the plasmonic emitter and the cell (d) is reduced from 1 mm to 10 nm. At nanoscale separation distance ($d < 100$ nm), both the frustrated modes in the InAs cell and the surface plasmon polaritons (SPPs) close to the surface of ITO are excited [33], which results the rise of the local ERRC at the front side of the InAs cell. At large separation distance ($d > 100$ nm), the frustrated modes in the InAs film dominate the external luminescence, which results a shift-up from the black solid curve ($d = 1$ mm) to dashed blue curve ($d = 100$ nm). The SPPs excited on the surface of the gold lead to the rise of the local external radiative recombination coefficient at the back of the cell. Figure 4a shows the enhancement effect of the BGR structure on the spatial profile of the local ERRC for a near-field TPV cell. Compared to the TPV configuration, adding a BGR with a 10 nm vacuum gap can enhance photon tunneling effect due to the coupling of the SPPs on the surface of ITO and frustrated modes in the InAs film. The Fabry-Perot effect brought by the emitter and the BGR modify the spatial coherent pattern of the ERRC and result in an emission boost at the middle part of the InAs cell ($t = 150\text{-}350$ nm). The enhancement of the local ERRC brought by the SPPs of the backside gold film is much smaller than that brought by the SPPs of ITO, since the plasma frequency of ITO is intentionally designed to match with the bandgap of InAs. Also, the skin depth of the coupled SPPs and frustrated modes at the front side is larger than that at the back side of the cell. However, the enhancement due to SPPs on the backside is significant at far-field regime for

the TPV-BGR structure, which is shown in Fig. 2d. Figure 4b and 4c illustrate the spectral local external radiative recombination coefficients of TPV and TPV-BGR configuration. The strong photon tunnelling phenomenon can be seen at the front side of the cell for both configurations. At every wavelength and location, the TPV-BGR configuration possesses a higher spectral local ERRC representing a better luminescence capability than the TPV configuration.

C. Doping effect of narrow bandgap semiconductors

As a narrow bandgap semiconductor material, the energy states at the bottom of the conduction and valence band are easily populated by free carriers. As the electron or hole concentration increases beyond the effective density of states in the conduction or valence band due to heavy doping effect, the InAs become degenerate, where the Moss-Burstein shift should be taken into consideration in the process of interband transitions.[34,35] When the lower energy states of the conduction band or higher energy states of the valence band are filled, the interband transitions of the electrons at the valence band require photons with energies larger than bandgap. Therefore, the absorption coefficient due to interband transition is reduced when the doping level is increased. As a reverse process of interband absorption, the interband emission (radiative recombination) has the same behavior as the interband absorption coefficient. Shown in Fig. 5a, the spatial profile of the ERRC of a *p*-type InAs in the TPV-BGR configuration remains almost unchanged at a lightly doping level ($N_A < 10^{18} \text{ cm}^{-3}$). When the doping level increases from $N_A = 10^{18} \text{ cm}^{-3}$ to $N_A = N_v(300 \text{ K}) = 3.7 \times 10^{18} \text{ cm}^{-3}$, which is the effective density of states in the valence band at 300 K, the spatial profile of the local ERRC decreases relatively significant and the ERRC of the cell decreases from $6.9 \times 10^{-16} \text{ m}^3/\text{s}$ to $4.1 \times 10^{-16} \text{ m}^3/\text{s}$. To be noted, the local ERRC is also related with the IIQE based on Eq. (11). When the doping level increases, the numerator of the IIQE is reduced due to the Moss-Burstein shift. Based on the sum rule of dielectric function, the

nonradiative contribution (mainly the contribution from free carrier at the wavelength above the bandgap) to the dielectric function of InAs further reduce the IIQE. Theoretically speaking, the reduction of the local ERRC is on account of combination effect of the Moss-Burstein shift and free carriers vibration. Nevertheless, as shown in Fig. 5b, the IIQE doesn't change significantly even when the doping level is close to the effective density of states in the conduction band. Therefore, the Moss-Burstein shift is dominant effect on the reduction of local external radiative recombination at a heavily doped InAs cell.

D. Thermal radiation and nonthermal radiation of a near-field thermoradiative cell

Due to low doping condition and low cell working temperature, the IIQE of a InAs cell can be assumed to be zero at the frequency below the bandgap energy and unity at the frequency above the bandgap energy, respectively, which is also referred as the ideal IIQE assumption. It is a common and reasonable assumption for radiative energy converters made of the direct bandgap semiconductors with low doping levels. However, this assumption can cause substantial error when one is modeling the radiative energy converters made of heavily doped direct semiconductors even not necessary under degenerate conditions. The temperature effect on the IIQE of the heavily doped InAs is clearly illustrated in Fig. 6. As temperature increases, the bandgap of InAs is shrunk from 0.354 eV at 300 K to 0.273 eV at 600 K. As the temperature of InAs is increased, the effective density of states in the valence band increases proportional to $T^{3/2}$ [36]. Therefore, the doping level is also increasing as the temperature increases and the IIQE curves of higher temperatures approximate to 1 slower than that of lower temperatures as the photon frequency increases. For 300 K, the ideal IIQE assumption is rather reasonable. However, potential errors become inevitable if the ideal IIQE assumption is applied to a InAs cell in a near-field TR-BGR configuration, which is shown in the subplot in Fig. 7. Normally, for a TPV-BGR

configuration, the hot emitter made of tungsten and ITO is contacting with hot source with higher temperatures and the cell is supposed to contact with a heat sink to maintain at a lower temperature. By switching the hot side with the cold side, the TPV-BGR configuration is turned into a TR-BGR configuration. The side of *p*-type InAs with a BGR structure is fixed at 600 K, and the side of tungsten and ITO is fixed at 300K as shown in the subplot in Fig. 7. The photon chemical potential is fixed at -0.052 eV, which is corresponding to the maximum power condition of this TR cell. The ideal IIQE and real IIQE are used in the calculation to indicate that the ideal IIQE assumption can cause the substantial error of the net thermal and nonthermal emission. For a real IIQE, there should be two components of external emission: thermal emission and nonthermal emission. As the photon frequency increases, the IIQE approximates to unity indicating the interband transitions become dominant than the free carriers vibration. Therefore, the net thermal emission is decreasing as the photon frequency increases. When applying the ideal IIQE assumption, no thermal emission or absorption is existing above the bandgap energy of a InAs cell. The thermal contribution to the external emission is mistakenly turned into external luminescence. Hence, the total net nonthermal emission calculated by the ideal IIQE assumption is 7.4 kW/m^2 , which is overestimated by 11% compared to that calculated by real IIQE. This overestimation result in a critical difference when predicting the performance of the TR cell in this near-field TR-BGR configuration. As shown in Fig. 8, the maximum power predicted by ideal IIQE assumption is 1.04 kW/m^2 , while the real maximum power is only 0.923 kW/m^2 . Same observation can be made for the maximum efficiency. Note, the efficiency of the above TR-BGR configuration is not practical because this configuration and selected materials are optimized for a near-field TPV, but not for a near-field TR. However, the observations provide evidence to support our conclusion that capturing the

spatial effect and using the accurate value of IIQE are important parameters to accurately predict the performance of a thin-film near-field energy converter.

IV. CONCLUSIONS

Instead of using the generalized van Roosbroeck-Shockley model, this work demonstrates that fluctuational electrodynamics should be applied to fully capture various local effects on the external radiative recombination of thin-film radiative energy converters. Spatial effect due to multiple reflections and near-field radiation can significantly modify the local ERRC and increase the ERRC by several orders of magnitudes. One should consider the doping effect on the external radiative recombination only for a radiative energy converter consisting of heavily doped semiconductor, where the Moss-Burstein shift should also be considered. The thermal and nonthermal contributions to emission and absorption in a thin-film radiative energy converter are quantitatively distinguished. By comparing the predicted performance of a near-field TR-BGR configuration using a real IIQE and an ideal IIQE, we concluded that the IIQE is an important parameter to model a thin-film radiative energy converter.

ACKNOWLEDGEMENTS

D.F. and Z.M.Z. would like to thank the support from the U.S. Department of Energy (DOE), Office of Science, Basic Energy Sciences (DE-SC0018369). D.F. would also like to thank Dr. J.-J. Greffet for helpful discussion.

- [1] S. Basu, Z. M. Zhang, and C. J. Fu, *International Journal of Energy Research* **33**, 1203 (2009).
- [2] Z. M. Zhang, *Nano/Microscale Heat Transfer* (Springer Nature, Cham, 2020).
- [3] E. Tervo, E. Bagherisereshki, and Z. Zhang, *Frontiers in Energy* **12**, 5 (2018).
- [4] A. Fiorino, L. Zhu, D. Thompson, R. Mittapally, P. Reddy, and E. Meyhofer, *Nature Nanotechnology* **13**, 806 (2018).
- [5] R. Mittapally, B. Lee, L. Zhu, A. Reihani, J. W. Lim, D. Fan, S. R. Forrest, P. Reddy, and E. Meyhofer, *Nature Communications* **12**, 4364 (2021).
- [6] W.-C. Hsu, J. K. Tong, B. Liao, Y. Huang, S. V. Boriskina, and G. Chen, *Scientific Reports* **6**, 34837 (2016).
- [7] K. Chen, T. P. Xiao, P. Santhanam, E. Yablonovitch, and S. Fan, *Journal of Applied Physics* **122**, 143104 (2017).
- [8] L. Zhu, A. Fiorino, D. Thompson, R. Mittapally, E. Meyhofer, and P. Reddy, *Nature* **566**, 239 (2019).
- [9] S. Basu and Z. M. Zhang, *Applied Physics Letters* **95**, 133104 (2009).
- [10] B. Zhao, K. Chen, S. Buddhiraju, G. Bhatt, M. Lipson, and S. Fan, *Nano Energy* **41**, 344 (2017).
- [11] X. Liu and Z. M. Zhang, *Nano Energy* **26**, 353 (2016).
- [12] W. van Roosbroeck and W. Shockley, *Physical Review* **94**, 1558 (1954).
- [13] W. Shockley and H. J. Queisser, *Journal of Applied Physics* **32**, 510 (1961).
- [14] P. Würfel, *Journal of Physics C: Solid State Physics* **15**, 3967 (1982).
- [15] T. Trupke, M. A. Green, P. Würfel, P. P. Altermatt, A. Wang, J. Zhao, and R. Corkish, *Journal of Applied Physics* **94**, 4930 (2003).
- [16] J. DeSutter, R. Vaillon, and M. Francoeur, *Physical Review Applied* **8**, 014030 (2017).
- [17] A. Karalis and J. D. Joannopoulos, *Applied Physics Letters* **107**, 141108 (2015).
- [18] M. Francoeur and M. Pinar Mengüç, *Journal of Quantitative Spectroscopy and Radiative Transfer* **109**, 280 (2008).
- [19] J.-J. Greffet, P. Bouchon, G. Brucoli, and F. Marquier, *Physical Review X* **8**, 021008 (2018).
- [20] M. Francoeur, M. P. Mengüç, and R. Vaillon, *Journal of Physics D: Applied Physics* **43**, 075501 (2010).
- [21] D. Feng, E. J. Tervo, S. K. Yee, and Z. M. Zhang, *Nanoscale and Microscale Thermophysical Engineering* **24**, 1 (2020).
- [22] D. Feng, E. J. Tervo, D. Vasileska, S. K. Yee, A. Rohatgi, and Z. M. Zhang, *Journal of Applied Physics* **129**, 213101 (2021).
- [23] M. Francoeur, M. Pinar Mengüç, and R. Vaillon, *Journal of Quantitative Spectroscopy and Radiative Transfer* **110**, 2002 (2009).

- [24] W. A. Callahan, D. Feng, Z. M. Zhang, E. S. Toberer, A. J. Ferguson, and E. J. Tervo, *Physical Review Applied* **15**, 054035 (2021).
- [25] D. Milovich, J. Villa, E. Antolin, A. Datas, A. Marti, R. Vaillon, and M. Francoeur, *Journal of Photonics for Energy* **10**, 025503 (2020).
- [26] W. W. Anderson, *Infrared Physics* **20**, 363 (1980).
- [27] Z. Djuric, B. Livada, V. Jovic, M. Smiljanic, M. Matic, and Z. Lazic, *Infrared Physics* **29**, 1 (1989).
- [28] A. Martí, J. L. Balenzategui, and R. F. Reyna, *Journal of Applied Physics* **82**, 4067 (1997).
- [29] D. Feng, S. K. Yee, and Z. M. Zhang, arXiv preprint arXiv:2107.09772 (2021).
- [30] J. S. C. Prentice, *Journal of Physics D: Applied Physics* **33**, 3139 (2000).
- [31] T. Inoue, T. Suzuki, K. Ikeda, T. Asano, and S. Noda, *Opt. Express* **29**, 11133 (2021).
- [32] D. Fan, T. Burger, S. McSherry, B. Lee, A. Lenert, and S. R. Forrest, *Nature* **586**, 237 (2020).
- [33] B. Zhao, P. Santhanam, K. Chen, S. Buddhiraju, and S. Fan, *Nano Letters* **18**, 5224 (2018).
- [34] T. S. Moss, *Proceedings of the Physical Society. Section B* **67**, 775 (1954).
- [35] E. Burstein, *Physical Review* **93**, 632 (1954).
- [36] M. Levinshtein and S. Rumyantsev, *Handbook series on semiconductor parameters* (World Scientific, London, 1996), Vol. 1.

Figure captions

- Fig. 1. The ERRC of a InAs cell as a function of its film thickness.
- Fig. 2. (a) Spatial profile of the local ERRC of a cell in three different configurations at far-field regime. Spectral local ERRC of the InAs cell in (b) a cell configuration, (b) a far-field TPV configuration, and (c) a far-field TPV with a BGR configuration.
- Fig. 3. Spatial profile of the ERRC as a function of the vacuum gap distance of a near-field TPV cell with a BGR structure.
- Fig. 4. (a) Spatial profile of the local ERRC of the cell in a TPV and a TPV with a BGR structure. Spectral local external radiative recombination coefficient of the cell in (b) a cell configuration, (b) a far-field TPV configuration, and (c) a far-field TPV with a BGR configuration.
- Fig. 5. (a) Spatial profile of the local ERRC and (b) the IIQE of a near-field TPV cell with a BGR structure at different doping levels. $N_A = 3.7 \times 10^{18} \text{ cm}^{-3}$ is the boundary between a nondegenerate semiconductor and degenerate semiconductor for p-doped InAs at 300 K.
- Fig. 6. Intrinsic internal quantum efficiency of a InAs cell as a function of photon energy at different cell temperatures. The p -type InAs is fixed at the same value of effective density of states in the valence band at a given temperature, which is the boundary between a nondegenerate semiconductor and degenerate semiconductor for p -type InAs at that temperature.
- Fig. 7. Spectral heat flux of the net thermal and nonthermal emission of a p-doped InAs cell in a near-field TR device with a BGR structure. The doping level is intentionally chosen at $N_A = N_v(600 \text{ K})$ to clearly show the contribution of thermal radiation and nonthermal radiation. The InAs cell with the gold BGR is set at 600 K and the cold side is made of a bulk tungsten and ITO film, which are set at 300 K. This near-field TR device is operating at the maximum efficiency with a given

photon chemical potential ($\mu = -0.052$ eV). For the ideal IIQE assumption, no thermal radiation is emitted above the bandgap energy.

Fig. 8. The power-efficiency curve of a near-field TR device with a BGR structure. The device parameters are the same as Fig. 7. To be noted, nonradiative generation processes (Auger and SRH) are neglected here.

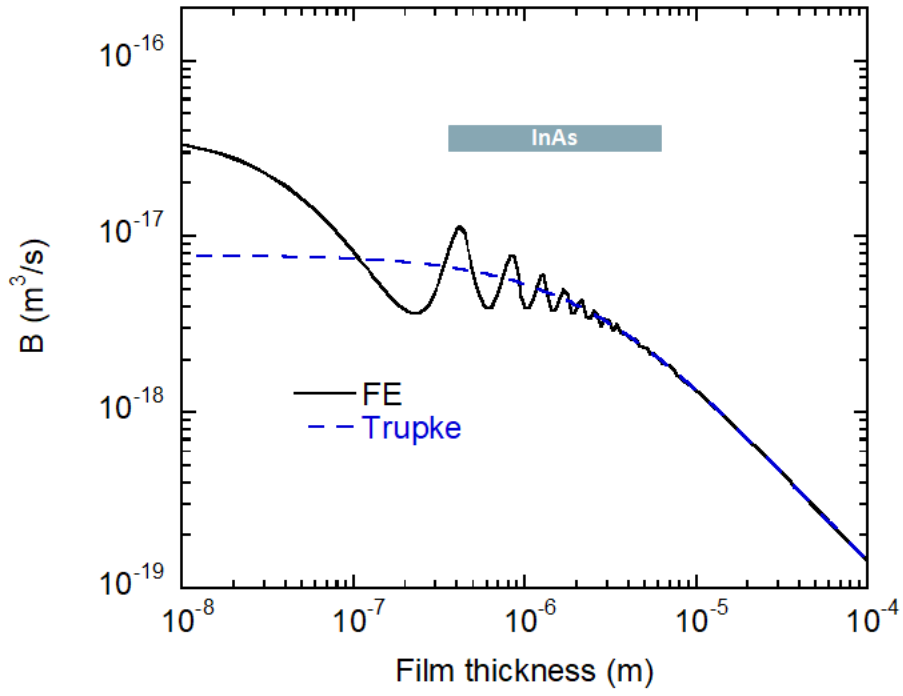


Fig. 1, Feng et al.

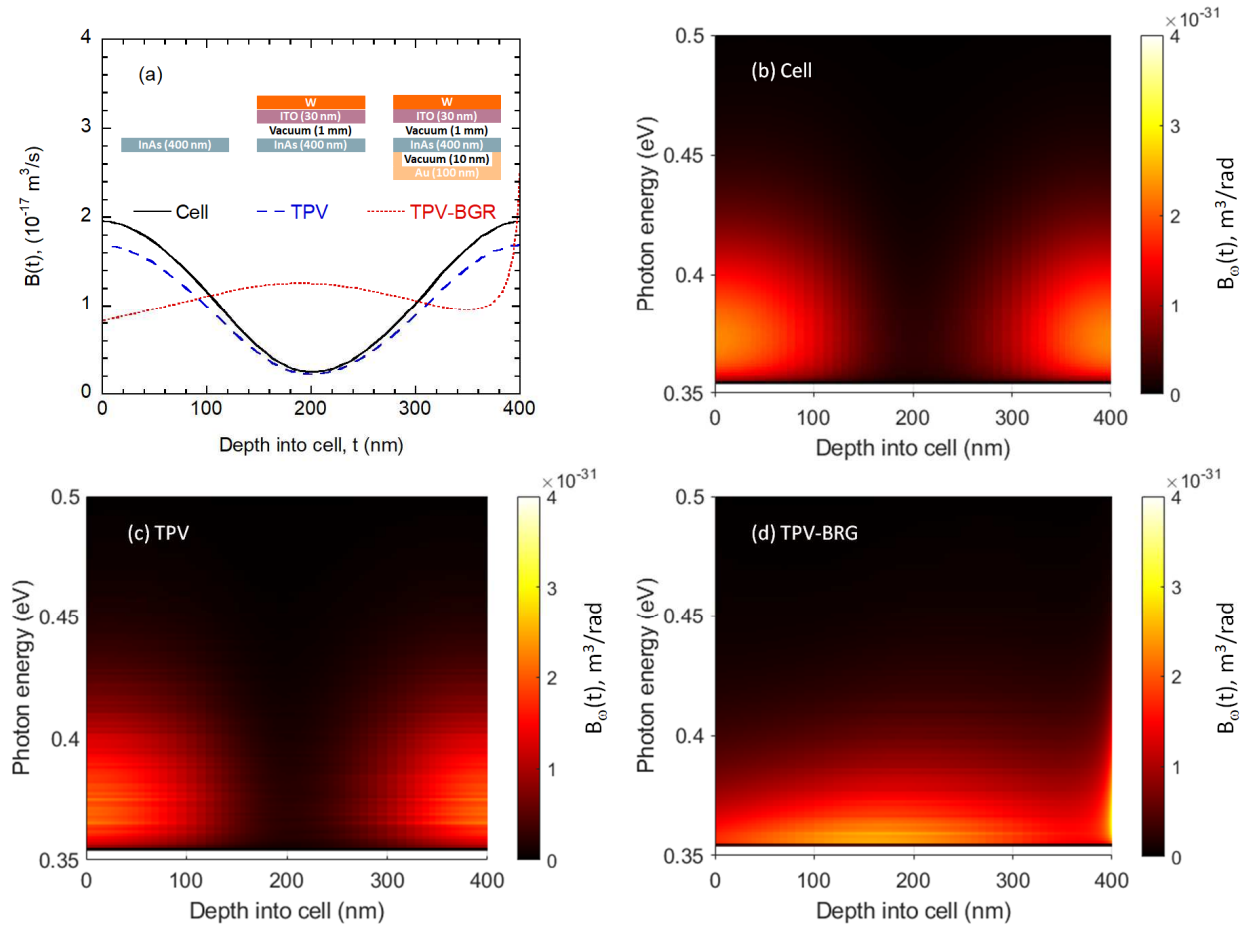


Fig. 2, Feng et al.

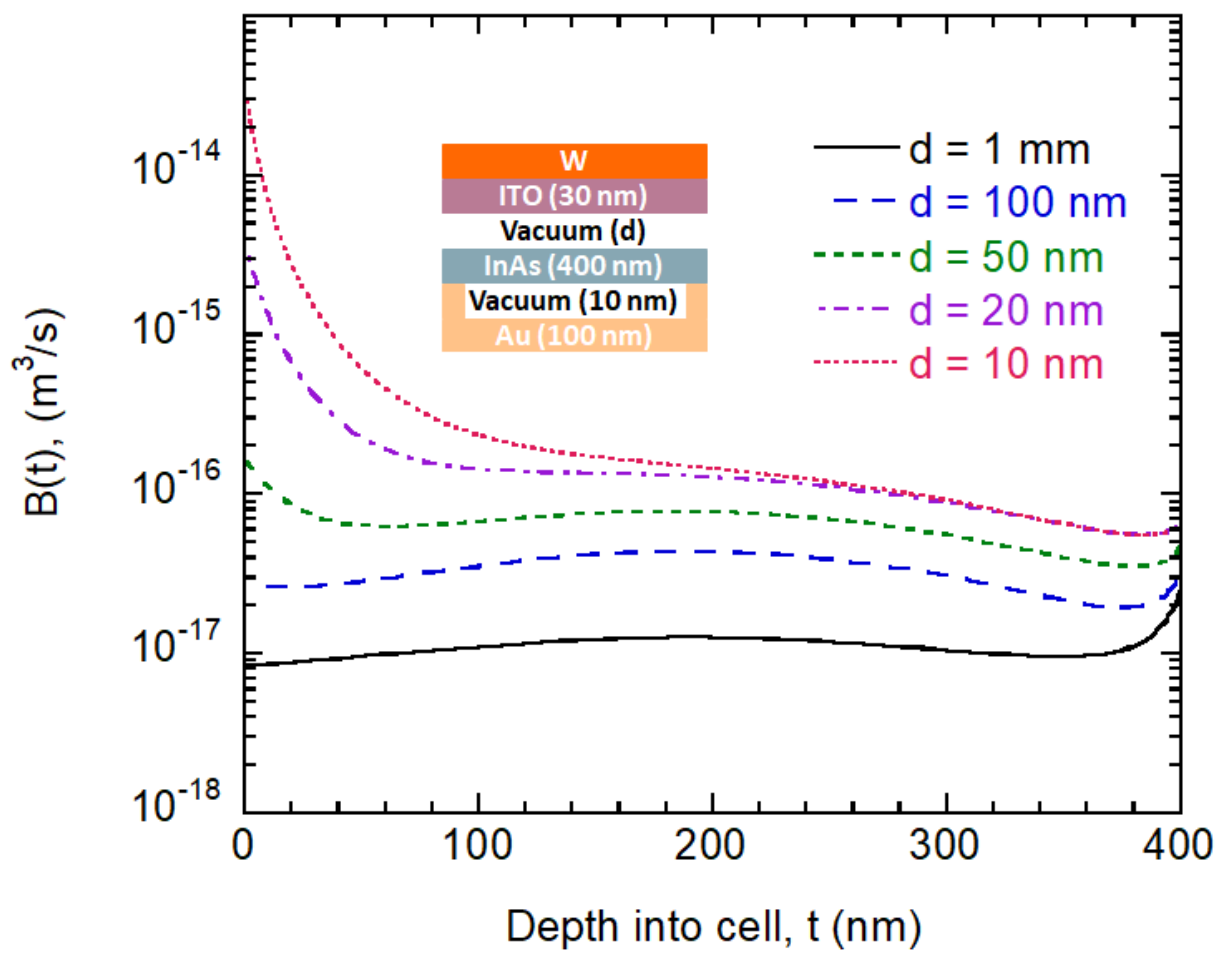


Fig. 3, Feng et al.

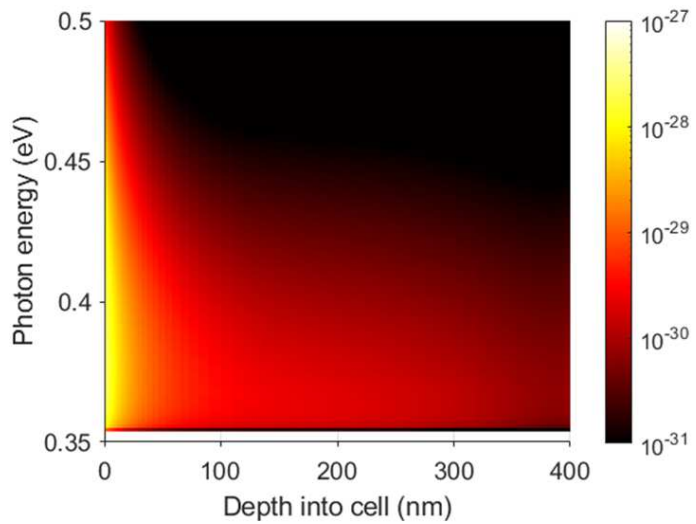
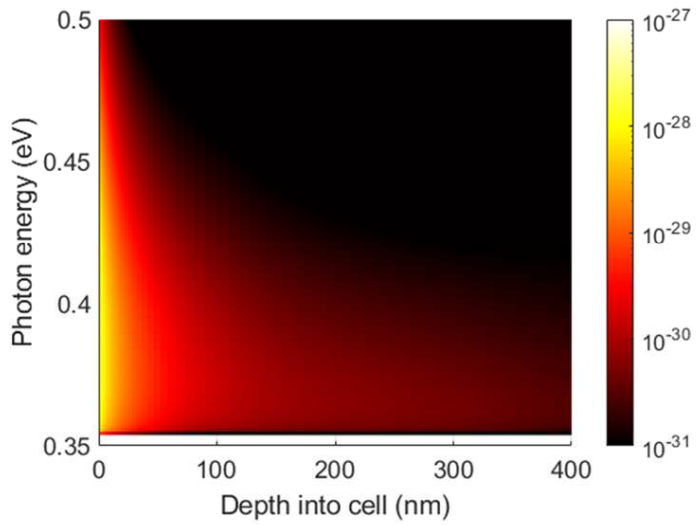
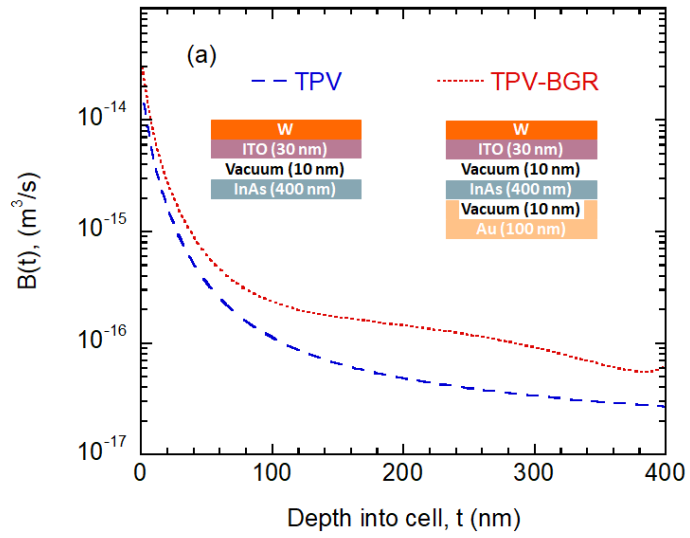


Fig. 4, Feng et al.

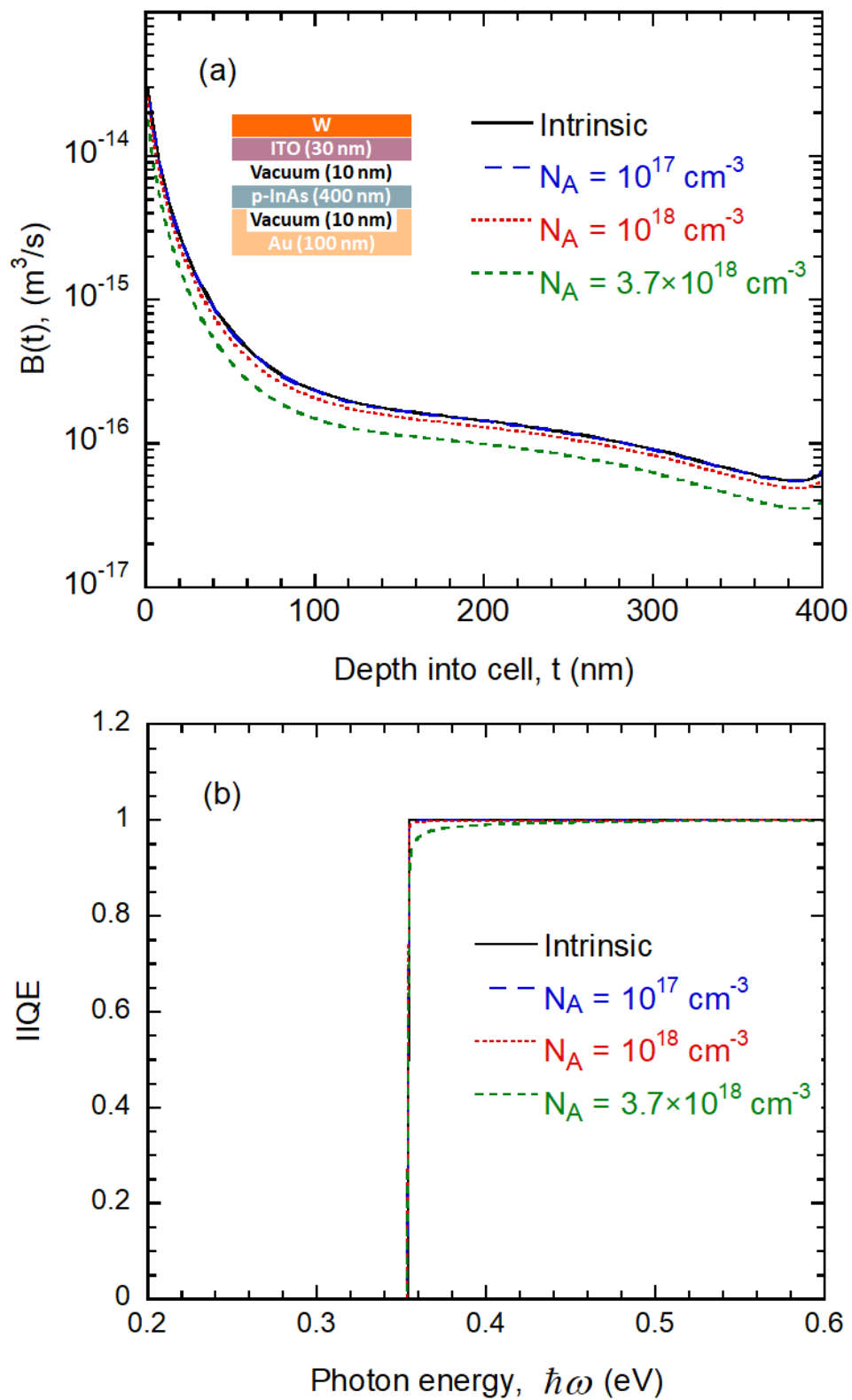


Fig. 5, Feng et al.

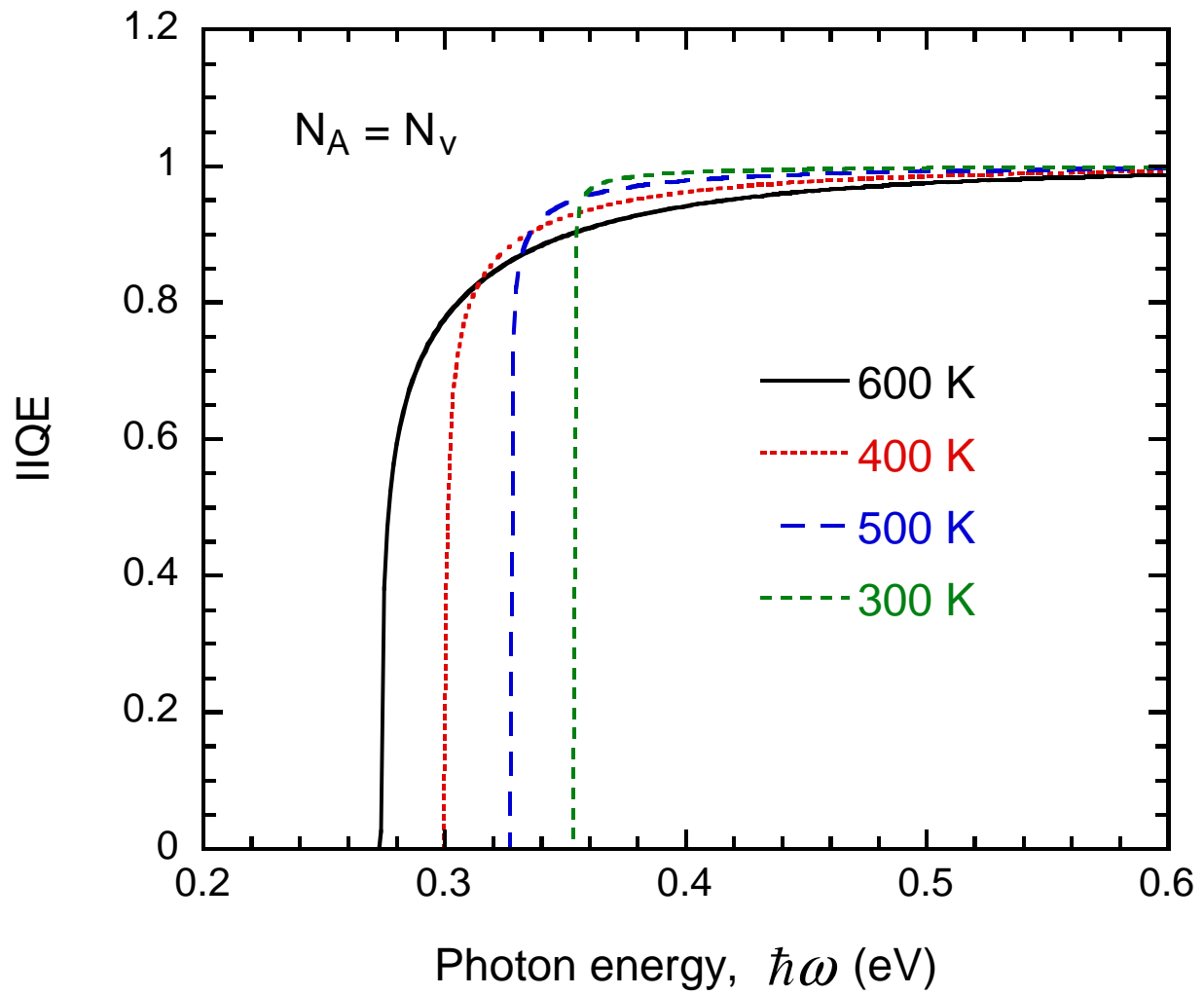


Fig. 6, Feng et al.

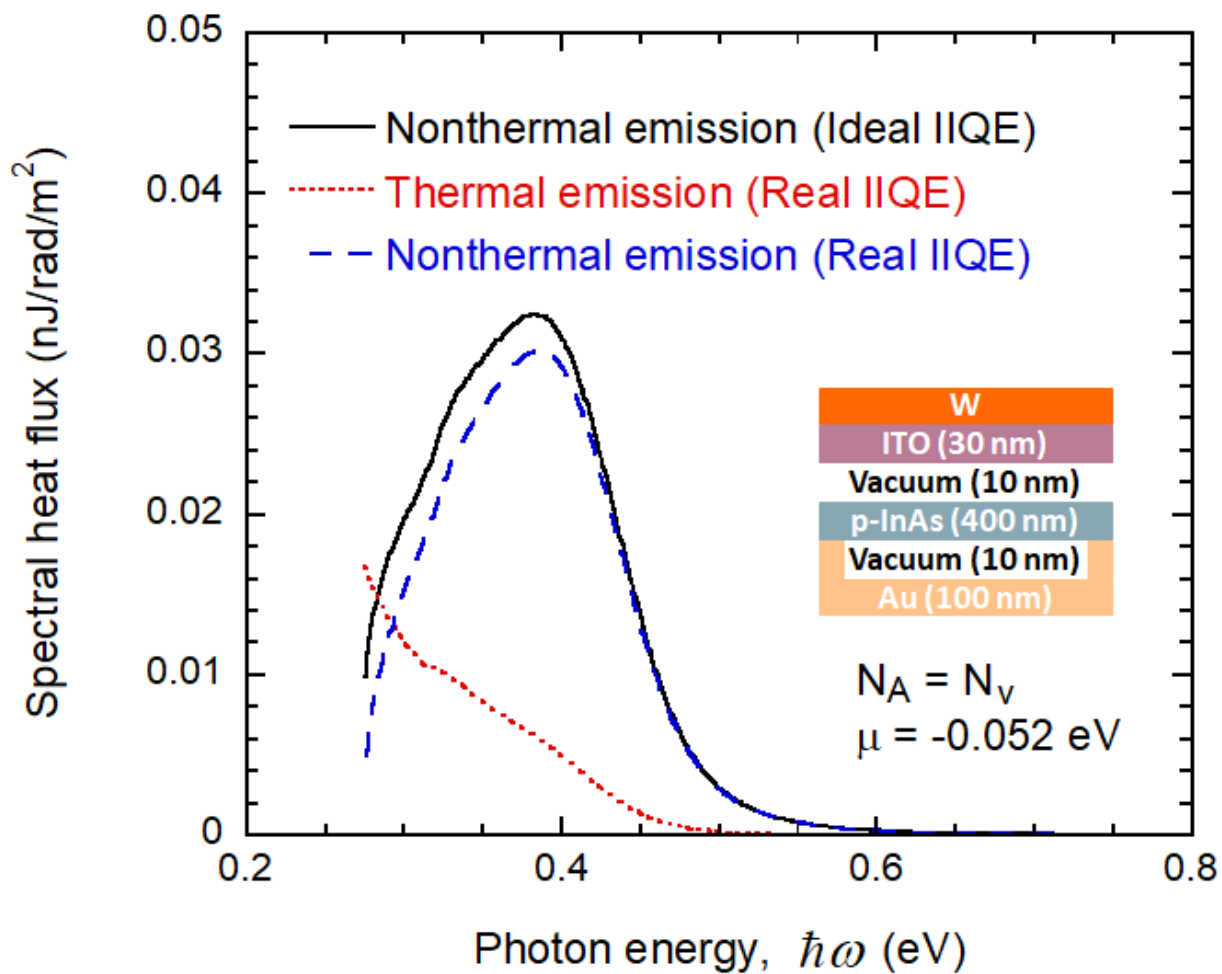


Fig. 7, Feng et al.

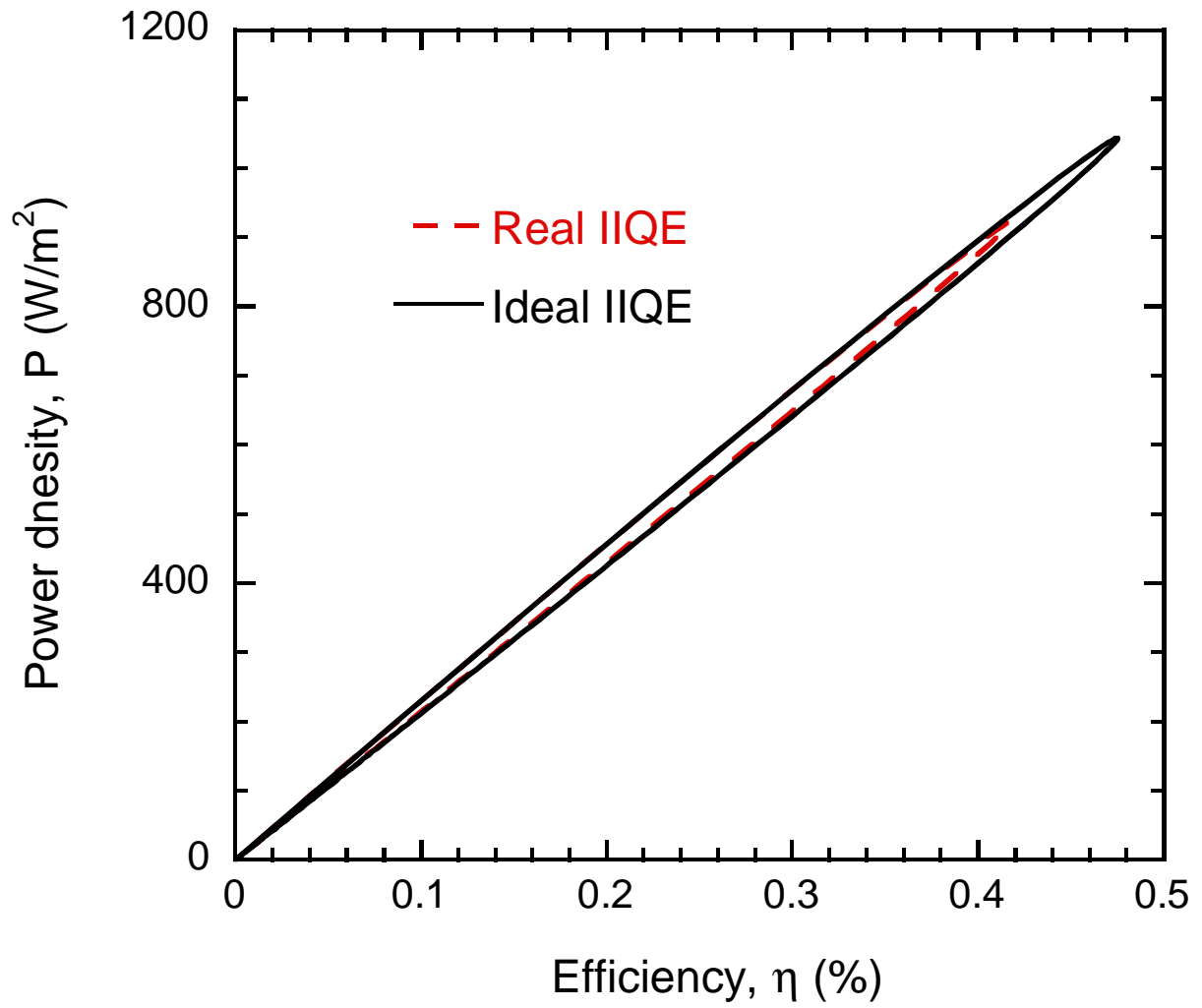


Fig. 8, Feng et al.